Effects of Slip and Chemical Reaction Models on Three-Dimensional Nonequilibrium Viscous Shock-Layer Flows

S. Swaminathan,* D. J. Song,* and Clark H. Lewis†
Virginia Polytechnic Institute and State University, Blacksburg, Virginia

Three-dimensional finite rate chemically reacting viscous shock-layer flows over complex geometries have been analyzed using seven- and eleven-species air models. The viscous shock-layer code for analyzing nonequilibrium flow over multiconics using a seven-species air model has been modified to include an eleven-species air model. The viscous shock-layer code with seven-species model has been modified to include wall-slip conditions, and the results for fully catalytic and noncatalytic surfaces with slip are presented. For the cases under consideration, the surface-measurable quantities computed using the two models agree well with each other. Wall slip had negligible effect on electron number density, whereas with shock slip, an order of magnitude increase in electron density was predicted.

Nomenclature

C_i = concentration of species i, ρ_i/ρ
CA = axial-force coefficient
CFSINF = skin friction coefficient in the streamwise direction
CI = C_i
E−/CC = electron concentration per cubic centimeter
FCW = fully catalytic wall
H = stagnation enthalpy, H^*/U_∞^2
NCW = noncatalytic wall
NEQ = finite rate nonequilibrium chemical reactions
PG = perfect gas
PINF = freestream pressure
PW = wall pressure
p = pressure, $p^*/\rho_\infty U_\infty^2$
q_w = heat transfer rate at the wall
Re = Reynolds number
Rn^* = nose radius, m
RN = Rn^*
SP = species
SS = shock slip
STINF = Stanton number, $q_w^*/\rho_\infty U_\infty (H_0^* - H_w^*)$
s, n, ϕ = nondimensional surface-oriented coordinate system
T = temperature, T^*/T_{ref}
T_{ref} = U_∞^2/C_{p_∞}
U_∞ = freestream velocity, m/s
u, v, w = velocity components
Y = distance normal to body
ZORN = z/Rn^*
z, Z = axial distance
α = angle of attack, deg
ϵ = Reynolds number parameter, $\epsilon^2 = \mu_{\text{ref}}/\rho_\infty U_\infty Rn^*$
μ = viscosity, μ^*/μ_{ref}
ξ, η, ζ = normalized surface-oriented coordinates
ρ = density, ρ^*/ρ_{ref}

Superscript

( )* = dimensional variable

Subscripts

i = species i
ref = dimensional reference conditions
w = wall conditions
∞ = dimensional freestream conditions
0 = stagnation conditions

Introduction

THE substantial improvements in the spacecraft performance achievable by aerobraking and aerocapture techniques have created considerable interest in the Aero-assisted Orbital Transfer Vehicle (AOTV). The aerobraking and aerocapture techniques are performed at high altitudes at reasonably high angles of attack. In contrast to re-entry vehicles, a substantial part of the flight of AOTV's occurs at high altitudes in the nonequilibrium flow regime. The velocities encountered in AOTV applications are relatively high, and the temperature levels attained in the shock layer are sufficiently high to ionize the oxygen and nitrogen molecules and atoms. For re-entry applications, a seven-species air model with single ionizing species has been used by many investigators, and the results generally agree well with the flight data. However, for AOTV applications, a seven-species model will be insufficient, since the ionization of oxygen and nitrogen atoms and molecules are not considered. In this paper, the effects of an eleven-species air model on the surface-measurable quantities and shock-layer profiles are studied. The viscous shock-layer code (VSLNEQ)[1,2] for analyzing straight and bent multiconics is modified to include an eleven-species air model, and the results are compared with those from the seven-species model. Results for perfect gas flow from a viscous shock-layer code (VSLET)[3] are presented for comparison.

At the altitudes at which the AOTV's operate, the low-density effects are very important, and proper slip conditions at the gas-wall interface must be considered. In this study, the slip conditions with wall catalysis for multicomponent nonequilibrium gas flow developed by Johnston and Hendricks[4] have been modified for three-dimensional flow and have been introduced into the seven-species code.

Two geometries have been used for the verification of the new method. The first is a sphere-cone-cylinder-flare with a nine-deg half-angle sphere-cone as the forebody (Fig. 1). The flare angle is 5 deg and the flare length is 10 nose radii. The

Presented as Paper 83-1425 at the AIAA 18th Thermophysics Conference, Montreal, Canada, June 1-3, 1983; received June 20, 1983; revision received Dec. 10, 1983.

*Graduate Student, Aerospace and Ocean Engineering Department. Student Member AIAA.

†Professor, Aerospace and Ocean Engineering Department. Associate Fellow AIAA.

nose radius is 0.1524 m (6 in.), and the cylindrical length is 10 nose radii. A freestream velocity of 7620 m/s (25,000 ft/s) and 83.82 km (275,000 ft) altitude conditions were used for this case. The wall temperature is maintained at 1000 K. The second geometry is a 10-deg half-angle sphere cone with a nose radius of 2.04 m (6.69 ft). This geometry has been analyzed at two altitude conditions for a freestream velocity of 9.8 km/s (32,152.2 ft/s). These conditions were chosen from Ref. 5. The details of the test conditions are given in Table 1.

Analysis

The viscous shock-layer equations are developed in a body-oriented orthogonal coordinate system (s, n, ϕ) where the s coordinate is tangent to the body in the streamwise direction, n is the coordinate normal to the surface, and the ϕ coordinate is the angle around the body measured from the windward streamline (see Fig. 2). The shock-layer equations were derived from the governing equations for reacting gas mixtures given by Bird et al.[6] or Williams.[7] The derivation of these equations and the solution procedure are described in detail in Refs. 8 and 9 and, hence, are not discussed here. In this section, the boundary conditions and the chemical reaction models used for the analysis are discussed in some detail. A brief discussion on the sources of thermodynamics and transport properties is also presented.

At the body surface, both slip and no-slip conditions can be imposed. The code can be used to analyze cold wall and adiabatic wall conditions. For a cold wall, the temperature can be a constant or a specified variation. For low-density flows, the effects of temperature jump are considered. The wall can be fully catalytic, finite catalytic, or noncatalytic; in this paper, results for the fully catalytic and noncatalytic surfaces are presented. The details of wall boundary conditions are given in Ref. 10. The shock boundary conditions with slip are the modified Rankine-Hugoniot equations and are given in Ref. 1. The input shock was obtained from an inviscid code, NOL3D.[11,12]

The multicomponent gas mixture is considered to be a mixture of thermally perfect gases. Thermodynamic and transport properties of each species were calculated using the local temperature. The properties for the gas mixture were then determined in terms of the individual species properties. The enthalpy and specific heat data of the species were obtained from the thermodynamic data of Browne.[13-15] The viscosity of each of the individual species was obtained from Blottner[16] and Yos.[17] The thermal conductivity of the individual species was calculated from the Eucken semiempirical formula. With viscosity and thermal conductivity of the individual species known, the viscosity and thermal conductivity of the mixture were calculated using Wilkes semiempirical relations. In this work, the diffusion model is limited to binary diffusion.

In the present study, it is assumed that the fluid medium is a mixture of reacting species and that the chemical reactions proceed at a finite rate. The production terms occurring in the energy equation and the species conservation equations are obtained from the various chemical reactions among the individual species. The number of equations to be included in the chemical reaction model depends on the particular problem being considered. For most re-entry applications, the temperature in the shock layer is such that a seven-species reaction model with a single ionizing species represents the chemistry reasonably well. The seven species considered are O, O_2, N, N_2, NO, NO^+, and e^-. For high-energy flows encountered during AOTV applications, the temperatures in the shock layer reach as high as 15,000 K, and the ionization of atoms and molecules of oxygen and nitrogen must be considered. Under these conditions, and eleven-species model consisting of O, O_2, N, N_2, NO, NO^+, O^+, O_2^+, N^+, N_2^+ and e^- represents the reactions in the flowfield more accurately.

Seven-species and eleven-species chemical reaction models were considered for comparison purposes. Reaction rate data for the seven-species model were based on Blottner,[16] whereas the reaction rate data for the eleven-species model were obtained from Kang and Dunn,[18] who considered 26 reactions to represent the chemistry in the flowfield. The reactions and rate data for the seven- and eleven-species models are given in Tables 2 and 3, respectively.

Results and Discussion

Figure 3 shows the surface pressure distribution for case 1 at zero angle of attack. The nonequilibrium pressure on the flare is higher than the perfect gas pressure by about 20%. The surface pressure distribution computed using the eleven-species model compares well with that computed using the seven-species model. Figure 4 shows the surface heat-transfer distribution for case 1 at $\alpha = 0$ deg. The diffusion heat transfer on the flare is much higher than that on the rest of the body.

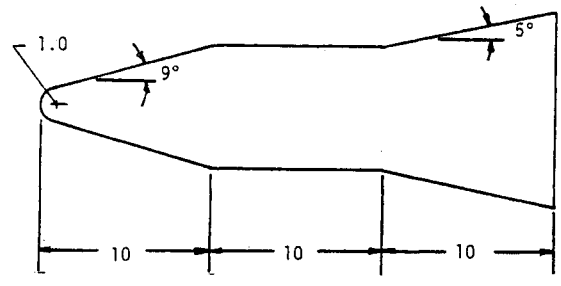

Fig. 1 Sphere-cone-cylinder-flare.

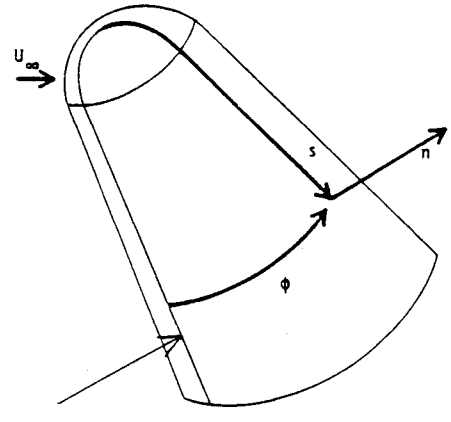

Fig. 2 Coordinate system.

Table 1 Test case conditions

			Freestream conditions					
Case	Rn, m	α	Alt, m	U_∞, m/s	T_∞, K	$Re_{,Rn}$	ϵ	Tw, K
1	0.1524	0	83820	7620	182.16	937.36	0.1745	1000
2a	2.0400	0	90000	9800	182.57	5210.00	0.0839	1000
2b	2.0400	5	95000	9800	191.27	1965.30	0.1338	1000

Table 2 Reaction rate data for seven-species model after Blottner

Reaction rate constants

$k_{f_r} = T_k^{C2_r} \exp(C0_r - Cl_r/T_k)$
$k_{b_r} = T_k^{D2_r} \exp(D0_r - Dl_r/T_k)$ T_k, K

Reaction no.	$C0_r$	$\exp(C0)_r$	Cl_r	$C2_r$	$D0_r$	$\exp(D0_r)$	Dl_r	$D2_r$
$r=1$	42.7302	3.61×10^{18}	59,400	−1	35.6407	3.01×10^{15}	0	−1/2
2	39.7963	1.92×10^{17}	113,100	−1/2	36.9275	1.09×10^{16}	0	−1/2
3	52.0800	4.15×10^{22}	113,100	−3/2	49.1959	2.32×10^{21}	0	−3/2
4	47.4305	3.97×10^{20}	75,600	−3/2	46.0617	1.01×10^{20}	0	−3/2
5	21.8801	3.18×10^{9}	19,700	1	27.5933	9.63×10^{11}	3600	1/2
6	31.8431	6.75×10^{13}	37,500	0	30.3391	1.50×10^{13}	0	0
7	22.9238	9.03×10^{9}	32,400	1/2	44.3369	1.80×10^{19}	0	−1

Table 3 Reaction rate data for eleven species model after Kang and Dunn

No.	Reaction Forward direction	Forward rate coeff, k_F cm^3/mole s	Backward rate coeff, k_B cm^3 mole s OR cm^6/mole^2 s	Third body, M -
1	$O_2+M\rightarrow 2O+M$	$3.6\times10^{18}T^{-1.0}\exp(-5.95\times10^4/T)$	$3.0\times10^{15}T^{-0.5}$	N, NO
2	$N_2+M\rightarrow 2N+M$	$1.9\times10^{17}T^{-0.5}\exp(-1.13\times10^5/T)$	$1.1\times10^{16}T^{-0.5}$	O,NO,O_2
3	$NO+M\rightarrow N+O+M$	$3.9\times10^{20}T^{-1.5}\exp(-7.55\times10^4/T)$	$1.0\times10^{20}T^{-1.5}$	O_2, N_2
4	$O+NO\rightarrow N+O_2$	$3.2\times10^{9}T^{1}\exp(-1.97\times10^4/T)$	$1.3\times10^{10}T^{1.0}\exp(-3.58\times10^3/T)$	
5	$O+N_2\rightarrow N+NO$	$7.0\times10^{13}\exp(-3.8\times10^4/T)$	1.56×10^{13}	
6	$N+N_2\rightarrow N+N+N$	$4.085\times10^{22}T^{-1.5}\exp(-1.13\times10^5/T)$	$2.27\times10^{21}T^{-1.5}$	
7	$O+N\rightarrow NO^+ + e^-$	$(1.4\pm0.4)\times10^{6}T^{1.5}\exp(-3.19\times10^4/T)$	$(6.7\pm2.3)\times10^{21}T^{-1.5}$	
8	$O+e^-\rightarrow O^+ + e^- + e^-$	$(3.6\pm1.2)\times10^{31}T^{-2.91}\exp(-1.58\times10^5/T)$	$(2.2\pm0.7)\times10^{40}T^{-4.5}$	
9	$N+e^-\rightarrow N^+ + e^- + e^-$	$(1.1\pm0.4)\times10^{32}T^{-3.14}\exp(-1.69\times10^5/T)$	$(2.2\pm0.7)\times10^{40}T^{-4.5}$	
10	$O+O\rightarrow O_2^+ + e^-$	$(1.6\pm0.4)\times10^{17}T^{-0.98}\exp(-8.08\times10^4/T)$	$(8.0\pm2.0)\times10^{21}T^{-1.5}$	
11	$O+O_2^+\rightarrow O_2+O^+$	$2.92\times10^{18}T^{-1.11}\exp(-2.8\times10^4/T)$	$7.8\times10^{11}T^{0.5}$	
12	$N_2+N^+\rightarrow N+N_2^+$	$2.02\times10^{11}T^{0.81}\exp(-1.3\times10^4/T)$	$7.8\times10^{11}T^{0.5}$	
13	$N+N\rightarrow N_2^+ + e^-$	$(1.4\pm0.3)\times10^{13}\exp(-6.78\times10^4/T)$	$(1.5\pm0.5)\times10^{22}T^{-1.5}$	
14	$O_2+N_2\rightarrow NO+NO^+ + e^-$	$1.38\times10^{20}T^{-1.84}\exp(-1.41\times10^5/T)$	$1.0\times10^{24}T^{-2.5}$	
15	$NO+N_2\rightarrow NO^+ + e^- + N_2$	$2.2\times10^{15}T^{-0.35}\exp(-1.08\times10^5/T)$	$2.2\times10^{26}T^{-2.5}$	
16	$O+NO^+\rightarrow NO+O^+$	$3.63\times10^{15}T^{-0.6}\exp(-5.08\times10^4/T)$	1.5×10^{13}	
17	$N_2+O^+\rightarrow O+N_2^+$	$3.4\times10^{19}T^{-2.0}\exp(-2.3\times10^4/T)$	$2.48\times10^{19}T^{-2.2}$	
18	$N+NO^+\rightarrow NO+N^+$	$1.0\times10^{19}T-^{0.93}\exp(-6.1\times10^4/T)$	4.8×10^{14}	
19	$O_2+NO^+\rightarrow NO+O_2^+$	$1.8\times10^{15}T^{0.17}\exp(-3.3\times10^4/T)$	$1.8\times10^{13}T^{0.5}$	
20	$O+NO^+\rightarrow O_2+N^+$	$1.34\times10^{13}T^{0.31}\exp(-7.727\times10^4/T)$	1.0×10^{14}	
21	$NO+O_2\rightarrow NO^+ + e^- + O_2$	$8.8\times10^{15}T^{-0.35}\exp(-1.08\times10^5/T)$	$8.8\times10^{26}T^{-2.5}$	
22	$O_2+O\rightarrow 2O+O$	$9.0\times10^{19}T^{-1.0}\exp(-5.95\times10^4/T)$	$7.5\times10^{16}T^{-0.5}$	
23	$O_2+O_2\rightarrow 2O+O_2$	$3.24\times10^{19}T^{-1.0}\exp(-5.95\times10^4/T)$	$2.7\times10^{16}T^{-0.5}$	
24	$O_2+N_2\rightarrow 2O+N_2$	$7.2\times10^{18}T^{-1.0}\exp(-5.95\times10^4/T)$	$6.0\times10^{15}T^{-0.5}$	
25	$N_2+N_2\rightarrow 2N+N_2$	$4.7\times10^{17}T^{-0.5}\exp(-1.13\times10^5/T)$	$2.72\times10^{16}T^{-0.5}$	
26	$NO+M\rightarrow N+O+M$	$7.8\times10^{20}T^{-1.5}\exp(-7.55\times10^4/T)$	$2.0\times10^{20}T^{-1.5}$	O,N,NO

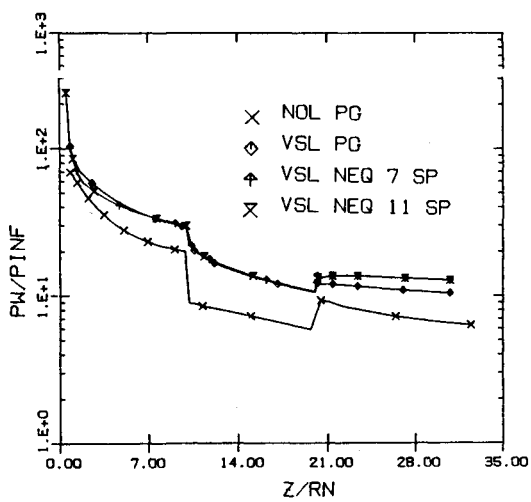

Fig. 3 Surface pressure distribution for case 1 at $\alpha = 0$ deg.

Table 4 shows the axial-force coefficient at $\alpha = 0$ deg for the two test cases. For case 1, the axial-force coefficient computed by the nonequilibrium code is about 15% higher than that computed by the perfect gas code. This was expected from the higher pressure on the flare predicted by the nonequilibrium code. The axial-force coefficients predicted by the seven- and eleven-species models are in good agreement.

Figures 5-9 show the shock-layer profiles for case 1 at a streamwise location of 8.8 nose radii. Figure 5 shows the electron number density computed by the present method using both seven- and eleven-species chemical reaction models. The results obtained by Kang and Dunn[18] using an integral method and experimental data from RAM C‡ flights are presented for comparison. RAM C flights were part of a program conducted by NASA Langley Research Center for

‡RAMC was a 9-deg half-angle spherically blunted cone flight tested by NASA.

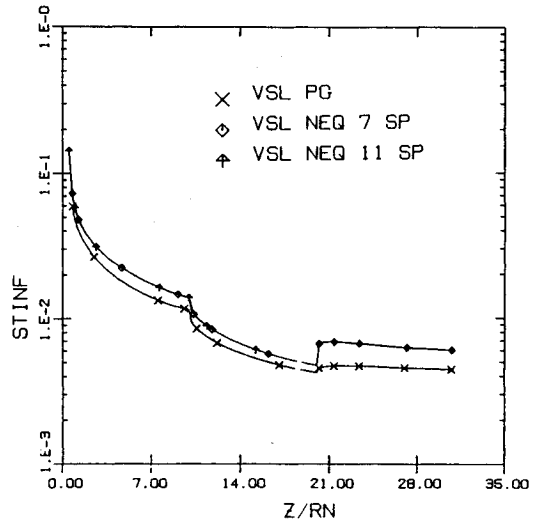

Fig. 4 Surface heat-transfer distribution for case 1 at $\alpha = 0$ deg.

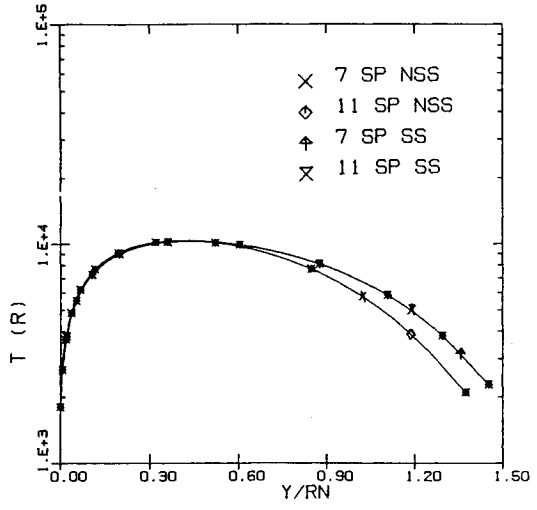

Fig. 6 Shock-layer temperature profile for case 1 at $s/Rn^* = 8.8$.

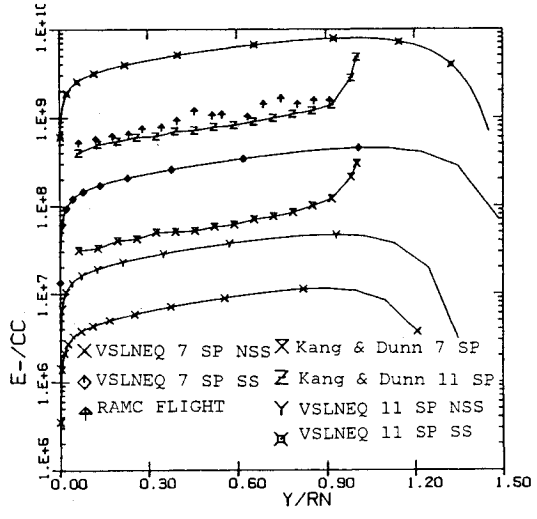

Fig. 5 Effect of chemical modeling on electron number density for case 1 at $s/Rn^* = 8.8$.

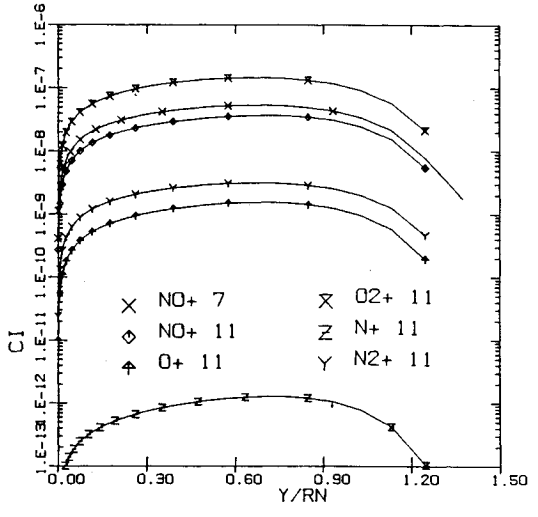

Fig. 7 Concentration of ionized species for case 1 at $s/Rn^* = 8.8$.

Table 4 Axial-force coefficients

Case	Code	Method	CA
1	NOL3D	PG	0.08718
1	VSL	PG	0.33334
1	VSL	NEQ 7 SP	0.38469
1	VSL	NEQ 11 SP	0.38505
2a	VSL	NEQ 7 SP	0.18176
2a	VSL	NEQ 11 SP	0.18198

studying flowfield electron concentration under re-entry conditions. The computations by the present method were performed for a fully catalytic wall. Without shock slip, the present method with the seven-species model considerably underpredicted the electron number density. The results from the present method using the eleven-species model were higher than those from the seven-species model. With shock slip, both the models predicted higher electron density. Without shock slip, the species concentrations behind the shock were the same as in the freestream, and thus the concentrations of both NO^+ and electrons were zero. With shock slip, however, a finite concentration of NO^+ was permitted behind the shock, and this nonzero concentration of NO^+ behind the shock raised the electron density profile. Also, with shock slip, both models predicted a thicker viscous shock layer and increased the static temperature (see Fig. 6). The increased temperature increased the ionization and hence higher electron density.

The eleven-species model considered five ionizing species. Each of these contributed to the electron density. Although the concentration of NO^+ predicted by the seven-species model was higher than that predicted by the eleven-species model, the concentration of O_2^+ is higher than that of NO^+ at these conditions (Fig. 7). The concentrations of O^+ and N_2^+ are an order or more lower than those of NO^+ and O_2^+ and, hence, have less influence on the electron density. The concentration on N^+ was a trace, explainable by the temperature levels attained in the shock layer. The maximum temperature in the shock layer was about 5500 K, and at these conditions the ionization of atoms is small. Also, by looking at the concentrations of the dissociated species (Fig. 8), it can be seen that there was little dissociation and, hence, fewer atoms were present to be ionized. This also explains the higher levels of O_2^+ and N_2^+. The predictions of dissociated atoms and the temperature profiles by both seven- and eleven-species model are in good agreement.

Comparing the electron density predicted by the present method with flight data shows that the seven-species model underpredicts the electron density, whereas the eleven-species

model overpredicts the flight data. Although the electron density predicted by the eleven-species model of Kang and Dunn is closer to the flight data in the shock layer, the upward swing near the shock and the peak at the shock cannot be explained. Since the maximum temperature in the shock layer is near the shock, not at the shock, the peak electron density occurs in the shock layer and decreases toward the shock. The present method predicted this trend correctly.

Figure 9 shows the effects of surface and wall boundary conditions on the electron number density for case 1 at $s/Rn^* = 8.8$. Results are presented for wall slip and no-wall slip, with and without shock slip. Even though the surface for the RAM C test case is fully catalytic, results for a non-catalytic surface are presented to obtain an upper bound on electron number density. From the figure, it can be seen that wall slip has a negligible effect on the electron number density, whereas with shock slip, the electron number density increased by an order of magnitude. With wall slip, the electron number density for the noncatalytic surface increased by about 10%. For a fully catalytic wall, even less difference is observed. The electron number density for the noncatalytic surface is an order of magnitude higher than that for the fully catalytic surface.

Figures 10-13 show the surface-measurable quantities and shock-layer profiles at the stagnation point for case 2a. Figure 10 shows the surface pressure distribution. The agreement between the two models is good. The surface heat-transfer and streamwise skin-friction distributions for case 2a are shown in Figs. 11 and 12. The inclusion of additional species did not affect these quantities. Figure 13 shows the stagnation point concentration profiles for case 2a. The wall is assumed to be fully catalytic, and frozen shock crossing conditions are used at the shock; hence at the wall and shock, the mixture consists of O_2 and N_2. In the shock layer, the dissociation of O_2 is complete. The concentrations of O and O^+ are of the same order, whereas the concentration of N is about 10% of the mixture. The temperature near the shock is about 27,400 K, hence the concentration of ionized species increases toward the shock.

Figures 14 and 15 show the surface-measurable quantities for case 2b at an angle of attack of 5 deg. The surface pressure distribution computed using the eleven-species model agrees well with that of the seven-species model (see Fig. 14). The surface heat-transfer distributions for both windward and leeside planes are shown in Fig. 15. The agreement between the two models is good. For this case, the surface-measurable quantities are unaffected by the inclusion of additional ionizing species in the chemistry. A generalized conclusion of the fact that the surface-measurable quantities are invariant to the seven-species and eleven-species models can only be obtained by conducting extensive studies at different freestream conditions.

Table 5 shows the computing times for various test cases considered. The computing time is based on an IBM 370/3081, H = OPT2 compiler. The nonequilibrium seven-species solution for each case has been taken as a reference. Time ratios for each test case are also presented. In general,

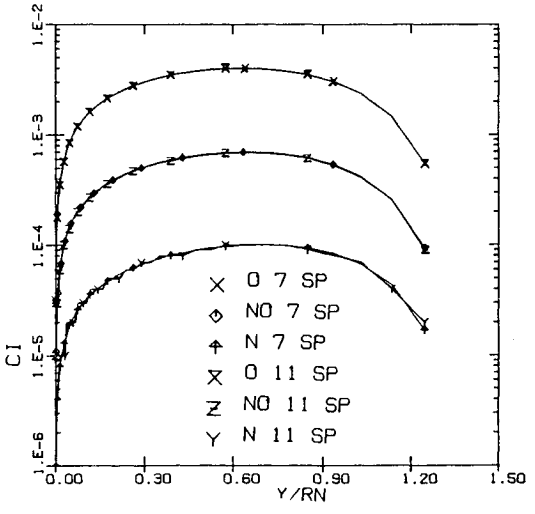

Fig. 8 Concentration of dissociated species for case 1 at $s/Rn^* = 8.8$.

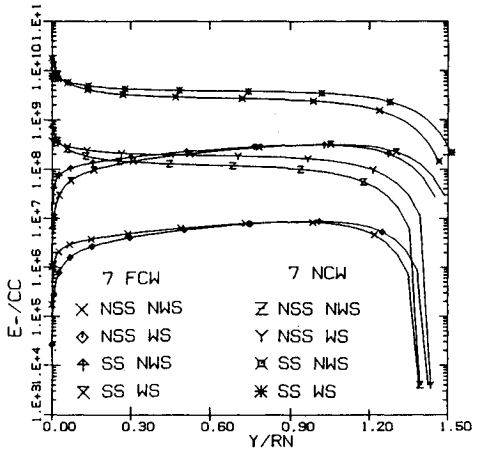

Fig. 9 Effect of boundary conditions on electron number density for case 1 at $s/Rn^* = 8.8$.

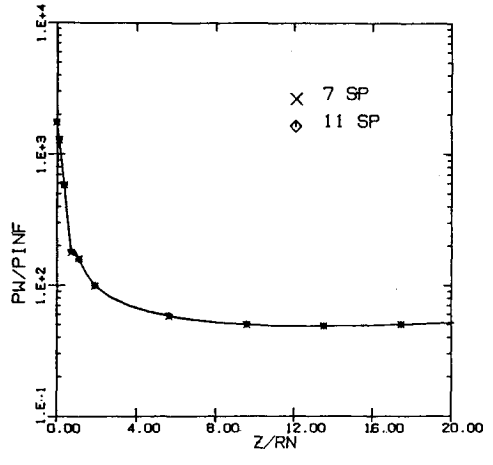

Fig. 10 Surface pressure distribution for case 2a at $\alpha = 0$ deg.

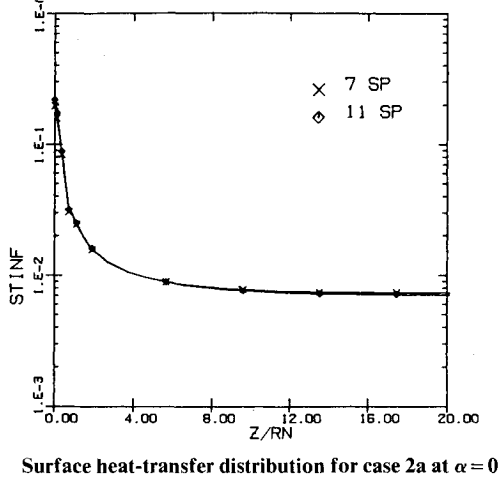

Fig. 11 Surface heat-transfer distribution for case 2a at $\alpha = 0$ deg.

Table 5 Computing times[a]

Case[b]		α, deg	ξ from – to	Grid size of ξ steps	η pts	ζ planes	Time m:s	Time ratio[c]
1	PG	0	0.0 – 31.5	70	101	1	0:28	1.00
1	NEQ	5	0.0 – 31.5	70	51	1	2:31	1.00
2a	NEQ 7	0	0.0 – 21.0	41	51	1	1:31	1.00
2a	NEQ 11	0	0.0 – 21.0	41	51	1	4:56	3.25
2b	NEQ 7	5	0.0-21.0	44	51	9	14:47	1.00
2b	NEQ 11	5	0.0 – 19.5[d]	41	51	9	40:00	2.75

[a]CPU time on IBM 370/3081, H = OPT2 compiler. [b]Case 1 = 9/0/5 Sphere-cone-cylinder-flare, case 2 = 10-deg sphere cone. [c]Nonequilibrium seven-species model is taken as reference. [d]Exceeded the initial time estimate.

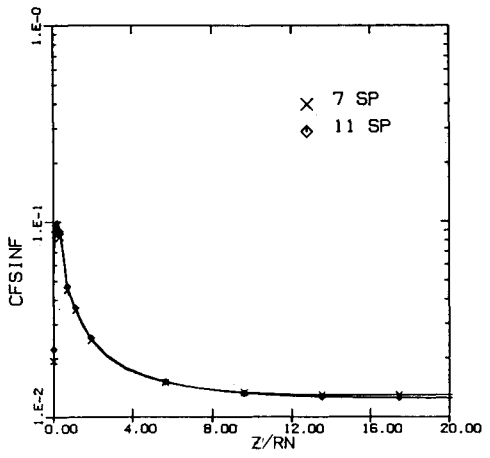

Fig. 12 Streamwise skin-friction distribution for case 2a at $\alpha = 0$ deg.

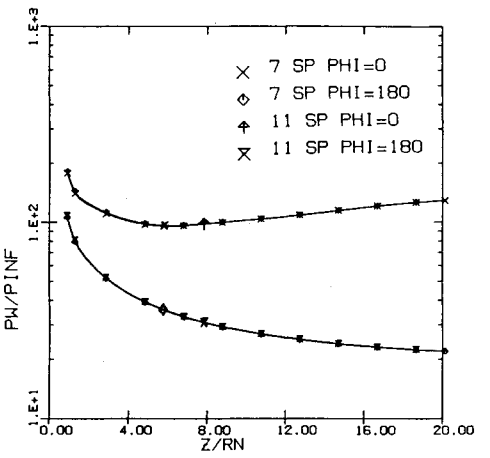

Fig. 14 Surface pressure distribution for case 2b at $\alpha = 5$ deg.

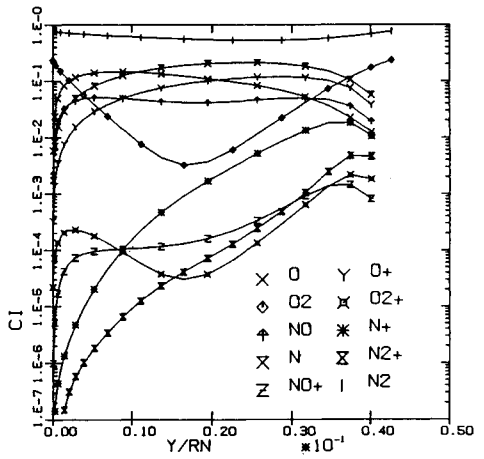

Fig. 13 Species concentration profiles at stagnation point for case 2a.

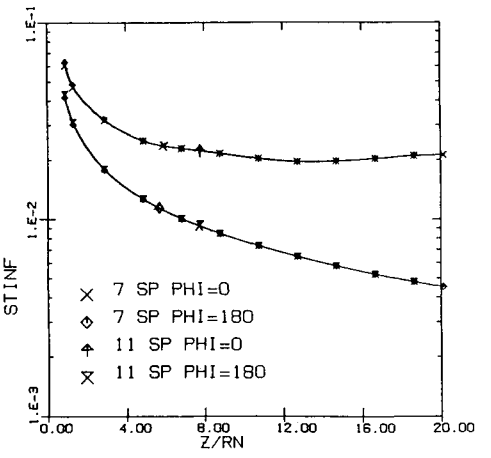

Fig. 15 Surface heat-transfer distribution for case 2b at $\alpha = 5$ deg.

the eleven-species model takes about three times the computing time required for the seven-species model. The seven-species nonequilibrium code, capable of solving multiconics and bent biconics, has a core requirement of 635 kbytes, whereas the eleven-species model needs only 690 kbytes.

Concluding Remarks

A numerical method for analyzing three-dimensional nonequilibrium flows over straight and bent multiconics using seven- and eleven-species chemical reaction models has been developed. The surface-measurable quantities computed using the eleven-species model agree very well with those computed using the seven-species model for the test cases considered. However, with the inclusion of additional ionizing species, the eleven-species model predicted a higher electron density. The axial-force coefficient for the sphere-cone-cylinder-flare at zero angle of attack predicted by the two nonequilibrium codes was in good agreement, and was about 15% higher than that for perfect gas flow.

Proper slip conditions with wall catalysis for three-dimensional, multicomponent nonequilibrium gas flow have been introduced in the seven-species code. Wall slip had negligible effect on the electron number density, whereas by including shock slip, the electron number density increased by

an order of magnitude. The electron number density for the noncatalytic surface was about an order of magnitude higher than that for the fully catalytic surface. In conclusion, a numerical method for analyzing nonequilibrium flows over straight and bent multiconics using seven- and eleven-species chemical reaction models in reasonable computing time is demonstrated.

References

[1]Swaminathan, S., Kim, M. D., and Lewis, C. H., "Nonequilibrium Viscous Shock-Layer Flows Over Blunt Sphere-Cones at Angle-of-Attack," AIAA Paper 82-0825, June 1982.

[2]Swaminathan, S., Kim, M. D., and Lewis, C. H., "Three-Dimensional Nonequilibrium Viscous Shock-Layer Flows Over Complex Geometries," AIAA Paper 83-0212, Jan. 1983.

[3]Thareja, R. R., Szema, K. Y., and Lewis, C. H., "Effects of Chemical Equilibrium on Three-Dimensional Viscous Shock-Layer Analysis of Hypersonic Laminar or Turbulent Flows," AIAA Paper 82-0305, Jan. 1982.

[4]Johnston, K. D. and Hendricks, W. L., "A Numerical Solution of the Navier-Stokes Equations for Chemically Nonequilibrium, Merged Stagnation Shock Layers on Spheres and Two-Dimensional Cylinders in Air," NASA TP 1227, May 1978.

[5]Menees, G. P., "Trajectory Analysis of Radiative Heating for Planetary Missions with Aerobraking of Spacecraft," AIAA Paper 83-0407, Jan. 1983.

[6]Bird, R. B., Stewart, W. E., and Lightfoot, E. N., *Transport Phenomena*, John Wiley and Sons, Inc., New York, 1960.

[7]Williams, F., *Combustion Theory*, Addison Wesley Book Co., Inc., Reading, Mass., 1965.

[8]Murray, A. L. and Lewis, C. H., "Three Dimensional Fully Viscous Shock-Layer Flows over Sphere-Cones at High Altitudes and High Angles of Attack," VPI-AERO-078, March 1975.

[9]Murray, A. L. and Lewis, C. H., "Hypersonic Three-Dimensional Viscous Shock-Layer Flow over Blunt Bodies," *AIAA Journal*, Vol. 16, Dec. 1978, pp. 1279-1286.

[10]Kim, M. D., "Three-Dimensional Nonequilibrium Viscous Shock-Layer Flow over the Space Shuttle Orbiter," Ph.D. Thesis, Virginia Polytechnic Institute and State University, Blacksburg, Va., April 1983.

[11]Solomon, J. M., Ciment, M., Ferguson, R. E., Bell, J. B., and Wardlaw, A. B. Jr., "A Program for Computing Steady Inviscid Three-Dimensional Supersonic Flow on Reentry Vehicles, Vol. I, Analysis and Programming," Report No. NSWC/WOL/TR 77-28, Feb. 1977.

[12]Solomon, J. M., Ciment, M., Ferguson, R. E., Bell, J. B., and Wardlaw, A. B. Jr., "A Program for Computing Steady Inviscid Three-Dimensional Supersonic Flow on Reentry Vehicles, Vol. II, User's Manual," NSWC/WOL/TR 77-28, Feb. 1977.

[13]Browne, W. G., "Thermodynamic Properties of Some Atoms and Atomic Ions," MSD Engineering Physics TM2, General Electric Co., Philadelphia, Pa., 1962.

[14]Browne, W. G., "Thermodynamic Properties of Some Diatomic and Linear Polyatomic Molecules," MSD Engineering Physics TM3, General Electric Co., Philadelphia, Pa., 1962.

[15]Browne, W. G., "Thermodynamic Properties of Some Diatoms and Diatomic Ions at High Temperature," MSD Advanced Aerospace Physics TM8, General Electric Co., Philadelphia, Pa., May 1962.

[16]Blottner, F. G., Johnson, M., and Ellis, M., "Chemically Reacting Viscous Flow Program for Multi-Component Gas Mixtures," Sandia Laboratories Report SC-RR-70-754, Dec. 1971.

[17]Yos, J. M., "Revised Transport Properties for High Temperature Air and its Components," Technical Release, Space Systems Division, Avco Corp., Wilmington, Mass., Nov. 28, 1967.

[18]Kang, S. W. and Dunn, M. G., "Theoretical and Experimental Studies of Reentry Plasmas," NASA CR-2232, April 1973.